Excitons and excitonic fine structures in Si nanowires: Prediction of an electronic state crossover with diameter changes

Lijun Zhang, Jun-Wei Luo, Alberto Franceschetti, and Alex Zunger

Phys. Rev. B **84**, 075404 — Published 1 August 2011

DOI: 10.1103/PhysRevB.84.075404

Exciton and Excitonic Fine Structure in Si Nanowires: Prediction of an Electronic State Crossover with Diameter Changes

Lijun Zhang, Jun-Wei Luo, Alberto Franceschetti, and Alex Zunger*
National Renewable Energy Laboratory, Golden, Colorado, USA 80401

Si nanowires have attracted considerable attention as promising candidates for electronic, thermoelectric, photonic, and photovoltaic devices, yet there appears to be only limited understanding of the underlying electronic and excitonic structures on all pertinent energy scales. Using atomistic pseudopotential calculations of single-particle as well as many-body states, we have identified remarkable properties of Si nanowires in three energy scales: (i) In the "*high energy*" $\sim$1 eV scale, we find an unusual electronic state crossover whereby the nature of the lowest unoccupied molecular orbital (LUMO) state changes its symmetry with wire diameters for [001]-oriented wires but not for [011]-oriented wires. This change leads to orbitally-allowed transitions becoming orbitally-forbidden below a certain critical diameter for [001] wires. (ii) In the "*intermediate energy*" $\sim 10^{-1}$ eV scale, we describe the excitonic binding, finding that in [001] wires the diameter (D) dependence of excitonic gap scales as $1/D^{1.9}$, not as $1/D^1$ as expected. The exciton binding energy increases from 52 meV at D=7.6 nm, to 85 meV at D=3.3 nm and 128 meV at D=2.2 nm. (iii) In the "*low energy*" $\sim 10^{-3}$ eV scale, we describe dark/bright excitonic states and predict how orbitally-allowed transitions (in scale (i)) become spin-forbidden due to the electron-hole exchange interaction, whereas the spin-allowed states in the orbitally-forbidden diameter region remain dark. The diameter dependence of the fine-structure splitting of excitonic states scales as $1/D^{2.3}$ in [001] wires and as $1/D^{2.6}$ in [011] wires. Surface-polarization effects are found to significantly enhance electron-hole Coulomb interaction, but have a small effect on the exchange fine-structure splitting. The present work provides a roadmap for a variety of electronic and optical effects in Si nanowires that can guide spectroscopic studies.

PACS numbers: 78.67.Lt, 73.21.Hb, 71.35.Cc, 78.20.Bh

Si nanowires have attracted considerable interest as promising candidate structures for electronic,[1,2] thermoelectric,[3,4] photonic,[5,6] and photovoltaic devices,[7–11] reflected by numerous papers on growth,[12–14] structural characterization,[15] transport[16,17] and optical[15,18–23] properties. Yet, there appears to be limited understanding of the underlying electronic and excitonic properties. Such understanding would span three energy scales: (i) in the "*high energy*" $\sim$1 eV scale one needs to understand the nature of confined energy levels and their dependence on wire orientation and diameter (single-particle physics); (ii) in the "*intermediate energy*" $\sim 10^{-1}$ eV scale one needs to understand the screened electron-hole Coulomb attraction which determines the exciton binding energy (many-body physics); and finally (iii) in the "*low energy*" $\sim 10^{-3}$ eV scale one encounters the electron-hole exchange interaction which splits the excitonic states into bright/dark states (many-body physics).

Current calculations and experiments on Si wires provide only limited understanding of the electronic and excitonic structures on all of these energy scales. On the theoretical side, in the $\sim$1 eV energy scale (i), density functional theory (DFT) calculations, which are computationally restricted to small-diameter wires, reported band structures for different wire orientations.[24–27] Since in DFT the bulk band gaps are often underestimated (by 60%) and the effective masses are overestimated (by 40%), the description of quantum confinement effects in nanowires is questionable. The semiempirical tight-binding method[28] was also used to probe scale (i). In the $\sim 10^{-1}$ eV energy scale (ii) the Bethe-Salpeter Equation (BSE) within the GW method was used to describe excitonic absorption,[29,30] yet GW-BSE calculations are computationally rather expensive, so large-diameter wires (>1.5 nm) were not considered and the spin-orbit (SO) coupling effect was generally ignored.[29,30] In the $\sim 10^{-3}$ eV energy scale (iii), the understanding is still dominated by simple exchange singlet-triplet splitting model based on two single-particle levels.[30,31] Furthermore, in an indirect-gap system such as Si the dark states are not only exchange-induced, but are affected by the symmetry of band-edge states and by intervalley coupling in the conduction bands.[32,33]

On the experimental side, scanning tunneling spectroscopy has been employed to evaluate the size-dependent quasiparticle band gaps in the scale (i). The gap increases from 1.1 eV at D=7.0 nm to 3.5 eV at D=1.3 nm.[15] As to scale (ii) and (iii), available photoluminescence spectra for Si nanowires show a complicated profile with relatively weak intensity compared to porous Si, broad peaks (the narrowest reported linewidth $\nu \sim 85$ meV at 7 K),[21] and long carrier decay time on the order of 1-$10^3 \mu$s.[20,34] These properties are strongly dependent on the wire size, morphology and surface passivation.[14,19,22,23] In this situation theoretical studies on excitonic properties of Si wires were usually compared to experimental results for porous Si,[29,30] which has a yet poorly understood morphology and interface.

Here we describe via explicit atomistic pseudopotential calculations a comprehensive analysis of Si nanowires along the [001] and [011] growth direction on all three energy scales. In scale (i) we find an unusual electronic state

crossover whereby the nature of the lowest unoccupied molecular orbital (LUMO) state changes its symmetry with wire diameter for [001] wires but not for [011]. This symmetry change leads to orbitally-allowed transitions becoming orbitally-forbidden below a certain critical diameter for [001] wires. In scale (ii) we describe the excitonic states of Si wires for different sizes and orientations, predicting the symmetry and polarization of the first few excitonic peaks. In [001] wires, the electronic state crossover noted above leads to distinct polarization behaviors of excitons for different diameter regions, whereas for [011] wires the excitonic structure is much simpler and the bright exciton is always polarized along the wire growth direction. In scale (iii) we predict how orbitally-allowed transitions (in scale (i)) become spin-forbidden due to the electron-hole exchange interaction, whereas spin-allowed states in the orbitally-forbidden diameter region are still dark. We also discussed the effect of surface-polarization induced by the dielectric mismatch between Si wire and the surrounding material. This study provides a roadmap for a variety of optical effects in Si nanowires that can guide spectroscopic studies of such systems.

Method. The single-particle electronic energies and wavefunctions (scale (i)) are calculated via the atomistic pseudopotential method described in Ref. 35. Briefly, the nanowire system is described by solving the Schrödinger equation:

$$[-\frac{\hbar^2}{2m}\bigtriangledown^2+\sum_{n,\alpha}v_\alpha(\mathbf{r}-\mathbf{R}_{n,\alpha})+\sum_\alpha V_\alpha^{SO}]\psi_i(\mathbf{r})=\epsilon_i\psi_i(\mathbf{r}), \tag{1}$$

where the Hamiltonian consists of the kinetic-energy (first term), the nanocrystal potential (second term), and the spin-orbit operator (third term). The nanocrystal potential specifies the atomistic symmetry as well as the mesoscopic shape and size of nanostructures, and is represented as a superposition of screened atomic pseudopotentials $v_\alpha(\mathbf{r}-\mathbf{R}_{n,\alpha})$ centered at the atom sites $\mathbf{R}_{n,\alpha}$. $v_\alpha(\mathbf{r}-\mathbf{R}_{n,\alpha})$ and V_α^{SO} are fitted to accurately reproduce the properties of bulk Si (band gap, critical energy levels, effective masses, deformation potentials, and spin-orbit splittings), thus correcting the well-known "DFT errors" for semiconductors. The Hamiltonian is diagonalized iteratively by expanding the wavefunction ($\psi_i(\mathbf{r})$ in Eq. 1) in plane waves, and selectively calculating band-edge states via the folded spectrum method.[36,37] The pseudopotential method naturally includes the effects of atomistic symmetry, quantum confinement, spin-orbit coupling, multiband coupling, and intervalley coupling (the last two originating from the lack of translational symmetry in nanostructures). Here the Si wires are constructed with circular cross-sections (except as noted) along the [001] and [011] direction and are embedded in a matrix material having a (variable) wide gap, mimicking various target surface passivations. Whereas other specific passivations have been used in the literature such as atomistic hydrogen H termination, we prefer here to capture a range of possible passivations by using a generic one.

The many-body excitonic properties (scale (ii) and (iii) above) are calculated within the framework of the screened configuration-interaction (CI) approach.[38] The exciton wavefunctions $|\Theta^{(\nu)}\rangle$ are expanded in terms of linear combinations of Slater determinants $|\Phi_{h_i,e_j}\rangle$ (corresponding to the h_i-e_j electron-hole pair) constructed from the antisymmetrized products of single-particle wavefunctions $\psi_i(\mathbf{r})$ obtained from Eq. 1:

$$|\Theta^{(\nu)}\rangle=\sum_{h_i,e_j}C^{(\nu)}(h_i,e_j)|\Phi_{h_i,e_j}\rangle, \tag{2}$$

where the coefficients $C^{(\nu)}(h_i,e_j)$ are the eigenstates of the CI Hamiltonian constructed by using the electron-hole Coulomb ($J_{h_ie_j,h'_ie'_j}$) and exchange ($K_{h_ie_j,h'_ie'_j}$) integrals:

$$H_{h_ie_j,h'_ie'_j}\equiv\langle\Phi_{h_i,e_j}|H_{CI}|\Phi_{h'_i,e'_j}\rangle=(\epsilon_{e_j}-\epsilon_{h_i})\delta_{h_ih'_i}\delta_{e_je'_j}-J_{h_ie_j,h'_ie'_j}+K_{h_ie_j,h'_ie'_j}. \tag{3}$$

The eigenvalues are energies of excitons, E_X. The $J_{h_ie_j,h'_ie'_j}$ and $K_{h_ie_j,h'_ie'_j}$ are calculated by using the single-particle orbitals $\psi_i(\mathbf{r})$:

$$J_{h_ie_j,h'_ie'_j}=e^2\sum_{\sigma_1,\sigma_2}\int\int\frac{\psi^*_{h'_i}(\mathbf{r}_1,\sigma_1)\psi^*_{e'_j}(\mathbf{r}_2,\sigma_2)\psi_{h_i}(\mathbf{r}_1,\sigma_1)\psi_{e_j}(\mathbf{r}_2,\sigma_2)}{\overline{\varepsilon}(\mathbf{r}_1,\mathbf{r}_2)|\mathbf{r}_1-\mathbf{r}_2|}d\mathbf{r}_1d\mathbf{r}_2, \tag{4}$$

$$K_{h_ie_j,h'_ie'_j}=e^2\sum_{\sigma_1,\sigma_2}\int\int\frac{\psi^*_{h'_i}(\mathbf{r}_1,\sigma_1)\psi^*_{e_j}(\mathbf{r}_2,\sigma_2)\psi_{e'_j}(\mathbf{r}_1,\sigma_1)\psi_{h_i}(\mathbf{r}_2,\sigma_2)}{\overline{\varepsilon}(\mathbf{r}_1,\mathbf{r}_2)|\mathbf{r}_1-\mathbf{r}_2|}d\mathbf{r}_1d\mathbf{r}_2. \tag{5}$$

The screening for these integrals is described by a position-dependent and size-dependent screening function $\overline{\varepsilon}(\mathbf{r}_1, \mathbf{r}_2)$, which gives a physically smooth transition from short range (unscreened) to long range (screened).[38] To describe the electron-hole interaction for excitons, in the CI calculations the wires are periodically expanded along the growth direction with a length of ∼11 nm, which is more than twice of the exciton Bohr radius of bulk Si (∼4.9 nm). We use a large enough number of single-particle valence (>40) and conduction (>40) band states to converge our CI basis: the calculated excitonic energies E_X have a residual convergence error of less than 0.2 meV.

The optical absorption spectra including excitonic effect are calculated with the CI eigenstates of Eq. 3 by using Fermi's golden rule:

$$I(E) = \sum_{\nu} |\mathbf{M}_\nu|^2 exp[-(\frac{E - E_\nu}{\sigma})^2], \tag{6}$$

where $\mathbf{M}_\nu = \sum_{h_i,e_j} C^{(\nu)}(h_i, e_j) < \psi_{h_i}|\widehat{\mathbf{P}}|\psi_{e_j} >$, is the dipole transition matrix, E_ν is the exciton energy and the broadening of spectral lines, σ is chosen as 50 μeV. The exciton decay lifetime (τ_ν) is calculated according to:[39]

$$\frac{1}{\tau_\nu} = \frac{4\alpha E_\nu n |M_\nu|^2}{m_0^2 \hbar c^2} \tag{7}$$

where n is the refractive index (∼ 4.0 for photon energies of 1-2 eV for Si),[40] α is the fine-structure constant, m_0 is the electron rest mass, and c is the velocity of light.

The dielectric mismatch between the nanostructure (dielectric constant ϵ_{in}) and its surrounding material (ϵ_{out}) will create image charges at the surface.[41] This leads to two additional contributions to the energies of excitons: (i) the self-energy correction (Σ_i^{pol}) of an electron (hole) in the single-particle state i, originating from the interaction between the electron (hole) and its own image charge; (ii) the Coulomb (exchange) interaction correction ($U^{\mathrm{pol}}_{h_i e_j, h_i' e_j'}$), originating from the mutual interaction of electron and hole, mediated by their image charges. The self-energy term is evaluated in first-order perturbation theory by:

$$\Sigma_i^{pol} = \int |\psi_i(\mathbf{r})|^2 \Sigma(\mathbf{r}) d\mathbf{r}, \tag{8}$$

where $\psi_i(\mathbf{r})$ is the single-particle wavefunction from Eq. 1 and the surface-polarization potential, $\Sigma(\mathbf{r})$ is numerically calculated as in Ref. 42. The Coulomb (exchange) interaction term is calculated via the electrostatic potential, $\Omega^{\mathrm{pol}}_{e_j, e_j'}(\mathbf{r})$,

$$U^{\mathrm{pol}}_{h_i e_j, h_i' e_j'} = e^2 \sum_\sigma \int \psi^*_{h_i}(\mathbf{r}, \sigma) \psi_{h_i'}(\mathbf{r}, \sigma) \Omega^{\mathrm{pol}}_{e_j, e_j'}(\mathbf{r}) d\mathbf{r}, \tag{9}$$

where $\Omega^{\mathrm{pol}}_{e_j, e_j'}(\mathbf{r})$ is the solution of the generalized Poisson equation,

$$\nabla \cdot \epsilon(\mathbf{r}) \nabla [\Omega^{\mathrm{dir}}_{e_j, e_j'}(\mathbf{r}) + \Omega^{\mathrm{pol}}_{e_j, e_j'}(\mathbf{r})] = -4\pi e^2 \sum_\sigma \psi^*_{e_j}(\mathbf{r}, \sigma) \psi_{e_j'}(\mathbf{r}, \sigma), \tag{10}$$

where the macroscopic dielectric constant $\epsilon(\mathbf{r})$ changes smoothly from ϵ_{in} to ϵ_{out} at the wire surface. $\Omega^{\mathrm{dir}}_{e_j, e_j'}(\mathbf{r})$ corresponds to the electrostatic potential excluding the surface-polarization effect, and is the solution of the Poisson equation,

$$\epsilon(\mathbf{r}) \nabla^2 \Omega^{\mathrm{dir}}_{e_j, e_j'}(\mathbf{r}) = -4\pi e^2 \sum_\sigma \psi^*_{e_j}(\mathbf{r}, \sigma) \psi_{e_j'}(\mathbf{r}, \sigma). \tag{11}$$

Eq. 10 and 11 are solved in real-space by using a finite-difference discretization of the gradient operator and a conjugate-gradient minimization algorithm.[42,43]

In the following we first present results for [001] wires from the above (i), (ii), and (iii) energy scales, and then show results for [011] wires. We then discuss the effects of dielectric mismatch on exciton binding and exchange interaction.

A. The *eV* energy scale: single-particle states. Bulk Si has six equivalent conduction band valleys Δ_X (along the Γ-X direction), from which the LUMO of wires derives. The confinement plane of [001] wires contains four of these six Δ_X valleys, folded to the $\bar{\Gamma}$ point of the wire Brillouin-zone. For [001] wires belonging to the D_{2d} point group, symmetry analysis[52] indicates that these four Δ_X-derived states correspond to the A_1, B_1, and E representation, where

both A_1 and B_1 are nondegenerate and E is doubly degenerate. The highest occupied molecular orbital (HOMO) always has nondegenerate B_2 symmetry for all wire sizes. Fig. 1(a) and 2 show evolution of the LUMO and HOMO state when the wire diameter is varied. At large diameter $D = 7.6$ nm, as quantum confinement and intervalley coupling are negligible, the splitting between A_1, B_1, and E is tiny, leaving all LUMO states practically degenerate. With decreasing diameters, the enhanced intervalley coupling lifts the degeneracy of these four states. This makes the B_1 state the lowest-energy one at diameter $D = 3.3$ nm to $D \sim 2.5$ nm (see Fig. 2). For lower diameters, the A_1 state becomes the LUMO (e.g. $D = 2.2$ nm in Fig. 1(a)). In contrast to the LUMO, the HOMO keeps the B_2 symmetry for all the diameters. These HOMO and LUMO states have characteristic wavefunctions corresponding to their specific symmetries, as shown in the right part of Fig. 1.

The switching of symmetry of the LUMO state with diameter has a strong effect on the optical properties of these wires. Table I shows the direct product $\langle h|\mathbf{P}_i|e\rangle$ for electron-hole dipole transition matrix elements, in terms of the irreducible representations of the D_{2d} group ($|e\rangle$ = A_1; B_1; E and $|h\rangle$ = B_2). The dipole operator $\mathbf{P}_i$ consists of two components: P_{001} representing photon polarized along the wire axis (along-wire), belonging to B_2 representation and P_{110} representing photon polarized perpendicular to the wire axis (in-plane), belonging to E representation. Any direct product having a symmetric A_1 representation is orbitally-allowed.[44] Thus, among all the HOMO→LUMO transitions for [001] wires, B_2→A_1 with the photon polarization P_{001} (along-wire) and B_2→E with P_{110} (in-plane) are orbitally-allowed, whereas B_2→B_1 is orbitally-forbidden. This symmetry analysis is consistent with our numerical calculations of the oscillator strength depicted in Fig. 1(b). At diameter $D = 7.6$ nm, we can see both B_2→A_1 (along-wire polarized) and B_2→E (in-plane polarized) transitions are orbitally-allowed, whereas the B_2→B_1 transition is orbitally-forbidden. With decreasing diameters, the LUMO symmetry changes from degenerate A_1+B_1+E (at $D = 7.7$ nm) to B_1 (at $D = 3.3$ nm) and finally to A_1 (at $D = 2.2$ nm). The optical transitions (Fig. 1(b)) show corresponding changes in polarization. At $D = 3.3$ nm the orbitally-forbidden B_2→B_1 transition is below the orbitally-allowed B_2→A_1 and B_2→E transitions, and then at $D = 2.2$ nm the orbitally-allowed B_2→A_1 transition emerges as the lowest-energy one with along-wire polarization. We also checked the above calculations for wires with square cross-section (also belonging to the D_{2d} point group) and obtain exactly the same symmetry-change sequence for the LUMO state. This indicates that the symmetry-change does not depend on slight modifications of the wire surface. It is an intrinsic property of the wire D_{2d} symmetry, which originates from the competition between quantum confinement and intervalley coupling. *Thus, we predict a confinement-induced electronic state crossover with diameter changes in [001] Si wires.* As shown below, this will result in corresponding transitions between different excitonic states.

B. Intermediate energy scale: exitonic states. Based on the group theory Table II describes how single-particle HOMO and LUMO states contribute to produce excitons. Here we convert single-group representations to corresponding double-group ones adding the spin degrees of freedom. It can be seen that three groups of excitonic states emerge from different symmetry of the LUMO state:

(1) At diameter $D = 7.6$ nm (Fig. 3(a)), the spin-orbit interaction splits the doubly degenerate LUMO E to Γ_6+Γ_6, and also transforms the HOMO B_2 to Γ_6. This $\Gamma_6 \otimes \Gamma_6$ manifold in principle should lead to two combinations of $A_1\oplus$ $A_2\oplus$ E excitonic states, of which the doubly degenerate E state is bright and in-plane polarized. However, due to very weak splitting of the two Γ_6 states (as a result of weak SO coupling), there is strong configuration mixing between these two $\Gamma_6 \otimes \Gamma_6$ exciton combinations, resulting in six lower-energy dark excitonic states and two upper bright states (in-plane polarized, labeled as transition "4") as described in Fig. 3(a).[53]

(2) At diameter $D = 3.3$ nm (Fig. 3(b)), the LUMO B_1 state is transformed to Γ_6, leading to $\Gamma_6 \otimes \Gamma_6 = A_1\oplus$ $A_2\oplus$ E excitonic states. The middle E state (labeled as transition "2") is bright with in-plane polarization.

(3) At diameter $D = 2.2$ nm (Fig. 3(c)), the LUMO A_1 state becomes Γ_7. When combined with the HOMO Γ_6, it generates the exciton combination $B_1\oplus$ $B_2\oplus$ E. The top B_2 (labeled as transition "3") and middle E state (labeled as transition "2") are bright with along-wire and in-plane polarization, respectively.

The calculated energy of the ground excitonic state (the lowest eigenvalue of Eq. 3), E_X are 1.182, 1.460, and 1.764 eV for $D = 7.6$ nm (B_2→E), 3.3nm (B_2→B_1), and 2.2 nm (B_2→A_1), respectively, as the E(1) listed in Table III. We fit the size dependence of E_X according to,

$$E_X = E_X^{bulk} + \frac{a}{D^\lambda}, \tag{12}$$

where $E_X^{bulk} = 1.1552$ eV[40] and D is the diameter, finding $a = 2.75$ and $\lambda = 1.90$. As expected from quantum confinement, the exciton binding energy (the energy difference between the single-particle band gap and the ground-state excitonic energy) is significantly enhanced from bulk Si (∼15 meV)[45] to Si wires, giving 52 meV (at $D = 7.6$ nm), 85 meV ($D = 3.3$ nm), and 128 meV ($D = 2.2$ nm).

C. Low 10^{-3} eV energy scale: bright/dark states *vs* fine-structure splittings. The absorption spectra shown on the right-hand side of Fig. 3 describe the bright/dark excitonic states caused by the exchange interaction and the intervalley coupling. For narrow wire of diameter $D = 2.2$ nm, the ground-state excitons originate from

the orbitally-allowed $B_2 \rightarrow A_1$ transition. The lowest one (B_1 symmetry) is dark (spin-forbidden), and higher states are spin-allowed — the middle semibright state (E, in-plane polarized) and the highest bright state (B_2, along-wire polarized). For medium wire of diameter D = 3.3 nm, the orbitally-forbidden $B_2 \otimes B_1$ is lower in energy than the other two orbitally-allowed combinations $B_2 \otimes A_1$ and $B_2 \otimes E$ and contributes to the ground-state excitons. In these excitons, the lowest (A_1) and highest (A_2) states are spin-forbidden and only the middle one (E) is spin-allowed. However even this spin-allowed state is generally dark, because it is orbitally-forbidden. At wide wire of diameter D = 7.6 nm, the bright in-plane polarized peak (labeled as transition "4") comes from the $B_2 \rightarrow E$ transition, which gives two spin-allowed excitons at the highest energy as mentioned. Also the exciton groups corresponding to $B_2 \rightarrow A_1$ and $B_2 \rightarrow B_1$ (all dark states) appear as ground-state excitons owing to the degeneracy of LUMO state. The absorption spectrum of D = 3.3 (Fig. 3(b)) and 2.2 nm (Fig. 3(c)) also shows the excited excitonic states at higher energies, which can be attributed to $B_2 \rightarrow (A_1/B_1/E)$ transitions.

The calculated exciton fine-structure splittings are listed in Table III. These are quite distinct from the results on Si quantum dots,[32] due to different degeneracy and symmetry of the LUMO and HOMO states. Fig. 4 shows the excitonic-gap dependence of the singlet-triplet splitting with no SO, Δ_{ST}, compared with previous GW+BSE results.[30] The wire diameter dependence of Δ_{ST} is found to scale as $1/D^{2.3}$. Previous GW+BSE calculations show much larger excitonic-gap energies and exchange splittings than ours at the same diameters, especially for the [001] wires. This could result from a high hydrogen coverage (high H-to-Si ratio) in their narrow wires: e.g. they used $Si_{25}H_{20}$ at D = 0.9 nm and $Si_{49}H_{28}$ at D = 1.4 nm for [001] wires.[29] The (cluster-connected) [001] wires require more H than (linear-chain-like) [011] wires,[27] and thus their electronic and excitonic properties are affected more by H-passivation than those of [011] wires. The Si-H bonding is known to modify Si enormously and H-passivation has been reported to result in much bigger band gaps than those with other passivations.[46] In the present work, the wire surfaces are passivated by generic large band-gap materials, and much larger diameter wires can be calculated.

We calculate the exciton decay time (τ_ν) for the bright excitonic states. At D = 3.3 nm, τ_ν of the transition "2" (Fig. 3(b)) is 1963.7 μs, as expected from its low oscillator strength since it is orbitally-forbidden (though spin-allowed). At D = 2.2 nm, τ_ν of transition "2" and transition "3" (Fig. 3(c)) are 77.2 and 1.6 μs. The long decay time is consistent with pseudodirect band-gap character of Si nanostructures and are reasonably within the range of experimentally measured 1-10^3 μs.[20,34]

Results for [011] wires. In [011] wires having the C_{2v} point group symmetry, two of the six equivalent bulk valleys Δ_X are projected to the confinement plane, and thus at large diameters the LUMO consists of only two degenerate states. In contrast to [001] wires, both of them belong to the A_1 representation, and thus no symmetry change of the LUMO state occurs with varying diameters. Fig. 5 shows the single-particle states and related optical transitions at D = 3.3 nm, and Table I gives the symmetry analysis of dipole matrix elements. Despite having the same symmetry, the two A_1 electron states show different wavefunctions. The HOMO has the B_1 symmetry, and thus all interband transitions ($B_1 \rightarrow A_1$) have along-wire polarization, P_{011} (Table I), as also confirmed by the calculated optical absorptions in Fig. 5(b).

Fig. 6 shows the excitonic structures generated from the HOMO and LUMO state. The corresponding symmetry analysis are given in Table II. The HOMO Γ_5 (from B_1) state and LUMO Γ_5 (from A_1) state produce the exciton combination of $A_1 \oplus A_2 \oplus B_1 \oplus B_2$. Among them the B_1 is a bright state with along-wire polarization, and A_1, B_2 are also bright with in-plane polarization. However, in the absorption spectra of Fig. 6 (right panel) we only can observe the bright B_1 exciton (labeled as transition "4") with the along-wire polarization, as the semidark A_1 (transition "2") and B_2 (transition "3") have two-order smaller oscillator strength. The ground-state excitonic energy is 1.335 eV (Table III) and the corresponding exciton binding energy is 66 meV. Both are smaller than those of the same size [001] wire due to weaker confinement as mentioned. The fine-structure splittings for the $B_1 \rightarrow A_1^{(1)}$ exciton group are listed in Table III. The excitonic-gap dependence of exchange splitting Δ_{ST} is shown in Fig. 4. The diameter dependence of Δ_{ST} scales as $1/D^{2.6}$, i.e. with a larger scaling factor than that of [001] wires. The calculated exciton decay time of the bright "4" state in Fig. 6 is 20.9 μs.

Effects of dielectric mismatch. Because nanowires are usually surrounded by materials with small dielectric constants (e.g. air, water, oxides, and organics), we studied the effects of dielectric mismatch by using $\epsilon_{\rm in}$ = 11.85[40] for the Si wire and $\epsilon_{\rm out}$ = 1∼5 for the surrounding material. The calculations are performed for the [001] wire with diameter D = 3.3 nm. Fig. 7 shows calculated surface-polarization potential $\Sigma(r)$. There is a sharp transition from positive to negative value near the wire surface, and the transition smears off with increasing $\epsilon_{\rm out}$. These are typical behaviors of surface-polarization potentials, also consistent with analytic expressions.[28,47,48]

The dielectric mismatch mainly contributes two opposite terms to the exciton energies (optical bandgap): the self-energy of the electron and the hole, which tends to increase the bandgap, and the electron-hole Coulomb interaction, which tends to decrease the bandgap. Fig. 8 shows the surface-polarization contribution to the self-energy ($\Sigma_{e1}^{\rm pol}$ + $\Sigma_{h1}^{\rm pol}$) and the Coulomb interaction (-$J_{e1,h1}^{\rm pol}$) as a function of $\epsilon_{\rm out}$. Both terms are remarkably enhanced for small values of $\epsilon_{\rm out}$. The correction from self-energy is significant: $\Sigma_{e1}^{\rm pol}$ + $\Sigma_{h1}^{\rm pol}$ reaches ∼400 meV at $\epsilon_{\rm out}$ = 1, which

agrees well with previous tight-binding result.[28] The enhancement of the exciton binding energy is also pronounced, as demonstrated in Ref. 47 and 48, e.g. $J^{\rm pol}_{e1,h1} \sim 250$ meV for $\epsilon_{\rm out} = 1$, by comparison with $J^{\rm dir}_{e1,h1} \sim 60$ meV. In three-dimensional quantum dots, it was demonstrated that $\Sigma^{\rm pol}_{e1} + \Sigma^{\rm pol}_{h1}$ and $J^{\rm pol}_{e1,h1}$ tend to cancel each other, and thus the surface-polarization has negligible effect on the optical bandgap.[43] In Si wires, the cancelation is not complete and the correction to the optical bandgap is positive. For other wires, negative (in CdSe)[49] and zero (in PbSe)[50] corrections were reported. The underlying mechanism is still under investigation and might be related to the different band structures and to the electron-to-hole effective mass ratio.[50]

Interestingly, we do not observe substantial change of the exchange interaction after including the dielectric mismatch, at least in our perturbative approach. The corresponding value of the exchange splitting, $K^{\rm pol}_{e1,h1}$ is less than 1 μeV. This demonstrates that the exchange interaction is predominantly enhanced by spatial confinement, not by dielectric mismatch. However, it should be mentioned that exciton localization near the wire axis induced by enhanced exciton binding ($J^{\rm pol}$) can lead to increased electron-hole exchange interaction. Another consequence of dielectric mismatch is the local-field effect, which leads to a strong suppression of lights polarized perpendicular to the wire axis within the framework of classical electromagnetic theory.[51] The evaluation of these effect is beyond the scope of this work.

Summary: We have presented a detailed study of electronic and excitonic properties on different energy scales for Si nanowires along the [001] and [011] growth direction. In the "high energy" single-particle energy scale, we predict an interesting electronic state crossover signaled by the switching of symmetry of the LUMO state with wire diameter for [001]-oriented wires (but not for [011]). This crossover leads to the formation of distinct exciton groups at different diameter regions in [001] wires. The orbitally-forbidden low-energy transitions in the medium-diameter region may result in a large Stokes shift, which can be probed experimentally. This result highlights the important role of intervalley coupling in determining electronic and optical properties of indirect band-gap nanomaterials. In the "low energy" many-body excitonic energy scale, we describe the excitonic states of Si wires for different sizes and orientation, and provide a systematic analysis of symmetry, polarization and fine-structure splitting of several excitonic lines. The size dependence of excitonic band gap, exciton binding energy, and exciton lifetime are calculated. The effects of dielectric mismatch on exciton binding energy and exchange splitting are discussed. The current study could be helpful for gaining insight into the electronic and optical properties of Si nanowires towards future optoelectronic applications.

Acknowledgement: L.Z. acknowledges helpful assistance on calculations from V. Popescu. This work is supported by the U.S. Department of Energy, Office of Science, Basic Energy Sciences, under Contract No. DE-AC36-08GO28308 to NREL.

* Corresponding Author: alex.zunger@gmail.com

[1] Y. Cui and C. M. Lieber, Science **291**, 851 (2001), ISSN 0036-8075.

[2] Y. Cui, Z. Zhong, D. Wang, W. U. Wang, and C. M. Lieber, Nano Lett. **3**, 149 (2003), http://pubs.acs.org/doi/pdf/10.1021/nl025875l, URL http://pubs.acs.org/doi/abs/10.1021/nl025875l.

[3] A. Hochbaum, R. Chen, R. Delgado, W. Liang, E. Garnett, M. Najarian, A. Majumdar, and P. Yang, Nature **451**, 163 (2008), ISSN 0028-0836.

[4] A. Boukai, Y. Bunimovich, J. Tahir-Kheli, J. Yu, W. Goddard Iii, and J. Heath, Nature **451**, 168 (2008), ISSN 0028-0836.

[5] M. Gudiksen, L. Lauhon, J. Wang, D. Smith, and C. Lieber, Nature **415**, 617 (2002), ISSN 0028-0836.

[6] R. Yan, D. Gargas, and P. Yang, Nature Photon. **3**, 569 (2009), ISSN 1749-4885.

[7] B. Tian, X. Zheng, T. Kempa, Y. Fang, N. Yu, G. Yu, J. Huang, and C. Lieber, Nature **449**, 885 (2007), ISSN 0028-0836.

[8] M. Kelzenberg, S. Boettcher, J. Petykiewicz, D. Turner-Evans, M. Putnam, E. Warren, J. Spurgeon, R. Briggs, N. Lewis, and H. Atwater, Nature Mater. **9**, 239 (2010), ISSN 1476-1122.

[9] E. C. Garnett and P. Yang, J. Am. Chem. Soc. **130**, 9224 (2008), pMID: 18576622, http://pubs.acs.org/doi/pdf/10.1021/ja8032907, URL http://pubs.acs.org/doi/abs/10.1021/ja8032907.

[10] L. Tsakalakos, J. Balch, J. Fronheiser, B. A. Korevaar, O. Sulima, and J. Rand, Appl. Phys. Lett. **91**, 233117 (2007).

[11] M. D. Kelzenberg, D. B. Turner-Evans, B. M. Kayes, M. A. Filler, M. C. Putnam, N. S. Lewis, and H. A. Atwater, Nano Lett. **8**, 710 (2008), pMID: 18269257, http://pubs.acs.org/doi/pdf/10.1021/nl072622p, URL http://pubs.acs.org/doi/abs/10.1021/nl072622p.

[12] Y. Cui, L. J. Lauhon, M. S. Gudiksen, J. Wang, and C. M. Lieber, Appl. Phys. Lett. **78**, 2214 (2001).

[13] J. B. Hannon, S. Kodambaka, F. M. Ross, and R. M. Tromp, Nature **440**, 69 (2006).

[14] J. D. Holmes, K. P. Johnston, R. C. Doty, and B. A. Korgel, Science **287**, 1471 (2000).

[15] D. D. D. Ma, C. S. Lee, F. C. K. Au, S. Y. Tong, and S. T. Lee, Science **299**, 1874 (2003).

[16] Y. Cui, X. Duan, J. Hu, and C. M. Lieber, J. Phys. Chem. B **104**, 5213 (2000), http://pubs.acs.org/doi/pdf/10.1021/jp0009305, URL http://pubs.acs.org/doi/abs/10.1021/jp0009305.

[17] H. Sellier, G. P. Lansbergen, J. Caro, S. Rogge, N. Collaert, I. Ferain, M. Jurczak, and S. Biesemans, Phys. Rev. Lett. **97**, 206805 (2006).

[18] J. Zhu, Z. Yu, G. F. Burkhard, C.-M. Hsu, S. T. Connor, Y. Xu, Q. Wang, M. McGehee, S. Fan, and Y. Cui, Nano Lett. **9**, 279 (2009), http://pubs.acs.org/doi/pdf/10.1021/nl802886y, URL http://pubs.acs.org/doi/abs/10.1021/nl802886y.

[19] D. P. Yu, Q. L. Hang, Y. Ding, H. Z. Zhang, Z. G. Bai, J. J. Wang, Y. H. Zou, W. Qian, G. C. Xiong, and S. Q. Feng, Appl. Phys. Lett. **73**, 3076 (1998), URL http://link.aip.org/link/?APL/73/3076/1.

[20] M. Dovrat, N. Arad, X.-H. Zhang, S.-T. Lee, and A. Sa'ar, Phys. Rev. B **75**, 205343 (2007).

[21] J. Qi, A. M. Belcher, and J. M. White, Appl. Phys. Lett. **82**, 2616 (2003), URL http://link.aip.org/link/?APL/82/2616/1.

[22] D. D. D. Ma, S. T. Lee, and J. Shinar, Appl. Phys. Lett. **87**, 033107 (pages 3) (2005), URL http://link.aip.org/link/?APL/87/033107/1.

[23] X. H. Sun, N. B. Wong, C. P. Li, S. T. Lee, and T. K. Sham, J. Appl. Phys. **96**, 3447 (2004), URL http://link.aip.org/link/?JAP/96/3447/1.

[24] A. J. Read, R. J. Needs, K. J. Nash, L. T. Canham, P. D. J. Calcott, and A. Qteish, Phys. Rev. Lett. **69**, 1232 (1992).

[25] X. Zhao, C. M. Wei, L. Yang, and M. Y. Chou, Phys. Rev. Lett. **92**, 236805 (2004).

[26] A. K. Singh, V. Kumar, R. Note, and Y. Kawazoe, Nano Lett. **6**, 920 (2006), http://pubs.acs.org/doi/pdf/10.1021/nl052505z, URL http://pubs.acs.org/doi/abs/10.1021/nl052505z.

[27] R. Rurali, Rev. Mod. Phys. **82**, 427 (2010).

[28] Y. M. Niquet, A. Lherbier, N. H. Quang, M. V. Fernández-Serra, X. Blase, and C. Delerue, Phys. Rev. B **73**, 165319 (2006).

[29] M. Bruno, M. Palummo, A. Marini, R. Del Sole, and S. Ossicini, Phys. Rev. Lett. **98**, 036807 (2007).

[30] M. Palummo, F. Iori, R. Del Sole, and S. Ossicini, Phys. Rev. B **81**, 121303 (2010).

[31] E. Martin, C. Delerue, G. Allan, and M. Lannoo, Phys. Rev. B **50**, 18258 (1994).

[32] F. A. Reboredo, A. Franceschetti, and A. Zunger, Phys. Rev. B **61**, 13073 (2000).

[33] T. Takagahara and K. Takeda, Phys. Rev. B **53**, R4205 (1996).

[34] M. Dovrat, Y. Shalibo, N. Arad, I. Popov, S.-T. Lee, and A. Sa'ar, Phys. Rev. B **79**, 125306 (2009).

[35] A. Zunger, *in Quantum Theory of Real Materials* (Kluwer, Boston, 1996).

[36] L. Wang and A. Zunger, J. Chem. Phys. **100**, 2394 (1994).

[37] L. W. Wang and A. Zunger, *in Semiconductor Nanoclusters* (Elsevier, New York, 1996).

[38] A. Franceschetti, H. Fu, L. W. Wang, and A. Zunger, Phys. Rev. B **60**, 1819 (1999).

[39] D. L. Dexter, *Solid State Physics* (Academic Press, New York, 1958).

[40] U. Rössler, ed., *Semiconductors: Group IV Elements, IV-IV and III-V Compunds* (Landolt-Börnstein, New Series, Group III, Vol. 41, Pt. a (Springer-Verlag, Berlin), 2001).

[41] L. E. Brus, The Journal of Chemical Physics **80**, 4403 (1984), URL http://link.aip.org/link/?JCP/80/4403/1.

[42] J. M. An, A. Franceschetti, and A. Zunger, Phys. Rev. B **76**, 045401 (2007).

[43] A. Franceschetti and A. Zunger, Phys. Rev. B **62**, 2614 (2000).

[44] P. Y. Yu and M. Cardona, *Fundamentals of semiconductors: physics and materials properties* (Springer-Verlag, Berlin, 2005), ISBN 3540254706.

[45] K. L. Shaklee and R. E. Nahory, Phys. Rev. Lett. **24**, 942 (1970).

[46] M. Nolan, S. O'Callaghan, G. Fagas, J. C. Greer, and T. Frauenheim, Nano Lett. **7**, 34 (2007), http://pubs.acs.org/doi/pdf/10.1021/nl061888d, URL `http://pubs.acs.org/doi/abs/10.1021/nl061888d`.
[47] E. A. Muljarov, E. A. Zhukov, V. S. Dneprovskii, and Y. Masumoto, Phys. Rev. B **62**, 7420 (2000).
[48] A. F. Slachmuylders, B. Partoens, W. Magnus, and F. M. Peeters, Phys. Rev. B **74**, 235321 (2006).
[49] A. Shabaev and A. L. Efros, Nano Letters **4**, 1821 (2004), http://pubs.acs.org/doi/pdf/10.1021/nl049216f, URL `http://pubs.acs.org/doi/abs/10.1021/nl049216f`.
[50] A. C. Bartnik, A. L. Efros, W.-K. Koh, C. B. Murray, and F. W. Wise, Phys. Rev. B **82**, 195313 (2010).
[51] J. Wang, M. S. Gudiksen, X. Duan, Y. Cui, and C. M. Lieber, Science **293**, 1455 (2001).
[52] For the calculations including spin-orbit (SO) coupling, strictly the double-group representations should be adopted for symmetry analysis instead of the single-group ones. Here for Si, the effect of SO coupling is not pronounced, e.g. there is only tiny splitting in energy for doubly degenerate E state with SO coupling. Thus for clarity and convention, we still perform the analysis using the single-group representations. We use the molecular notation, where A_1, A_2, B_1, B_2, and E correspond to Γ_1, Γ_2, Γ_3, Γ_4, and Γ_5 in the Koster notation.
[53] It should be mentioned that for such large-diameter wires, the LUMO is composed of degenerate A_1+B_1+E states, so all the three groups ($B_2 \rightarrow$E, $B_2 \rightarrow A_1$ and $B_2 \rightarrow B_1$) will appear as the ground-state excitons.

Figures

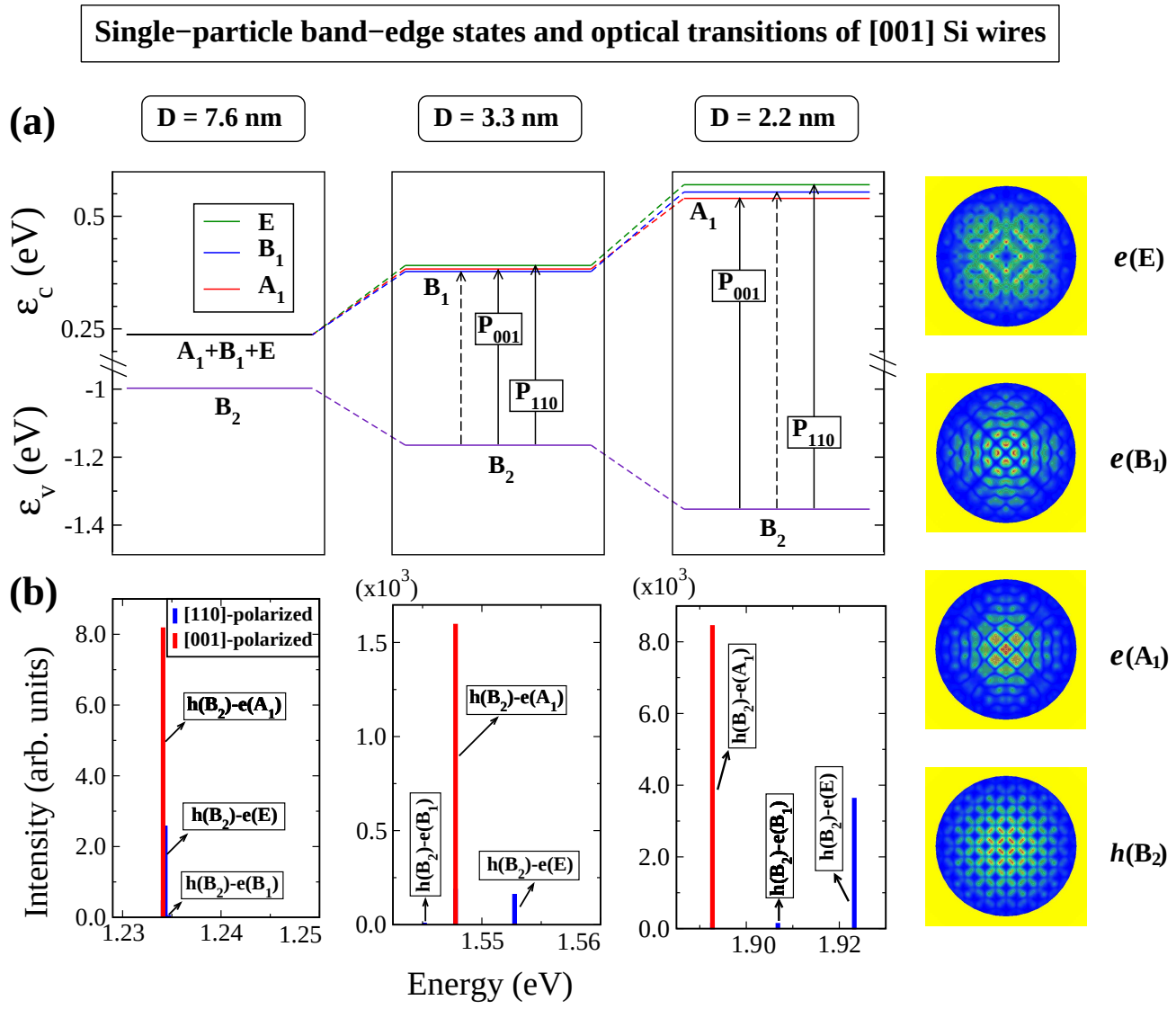

FIG. 1: (color online) Single-particle band-edge energy levels (a), wavefunction amplitudes (right panel), and corresponding optical transitions (b) for [001] Si wires of diameter D = 7.6, 3.3, and 2.2 nm. These diameters are chosen to represent three distinct size regimes with different optical transitions. The square of wavefunctions are shown for a D = 3.3 nm wire, with the plane intersecting the wire, perpendicular to the wire axis. The wire cross-sections are shown as blue circles. The dash arrow-lines represent orbitally-forbidden transitions whereas the solid arrow-lines correspond to orbitally-allowed transitions. Note that as a result of strong confinement, the oscillator strength for D = 3.3 nm and 2.2 nm are enhanced by two orders of magnitude compared with that for D = 7.6 nm.

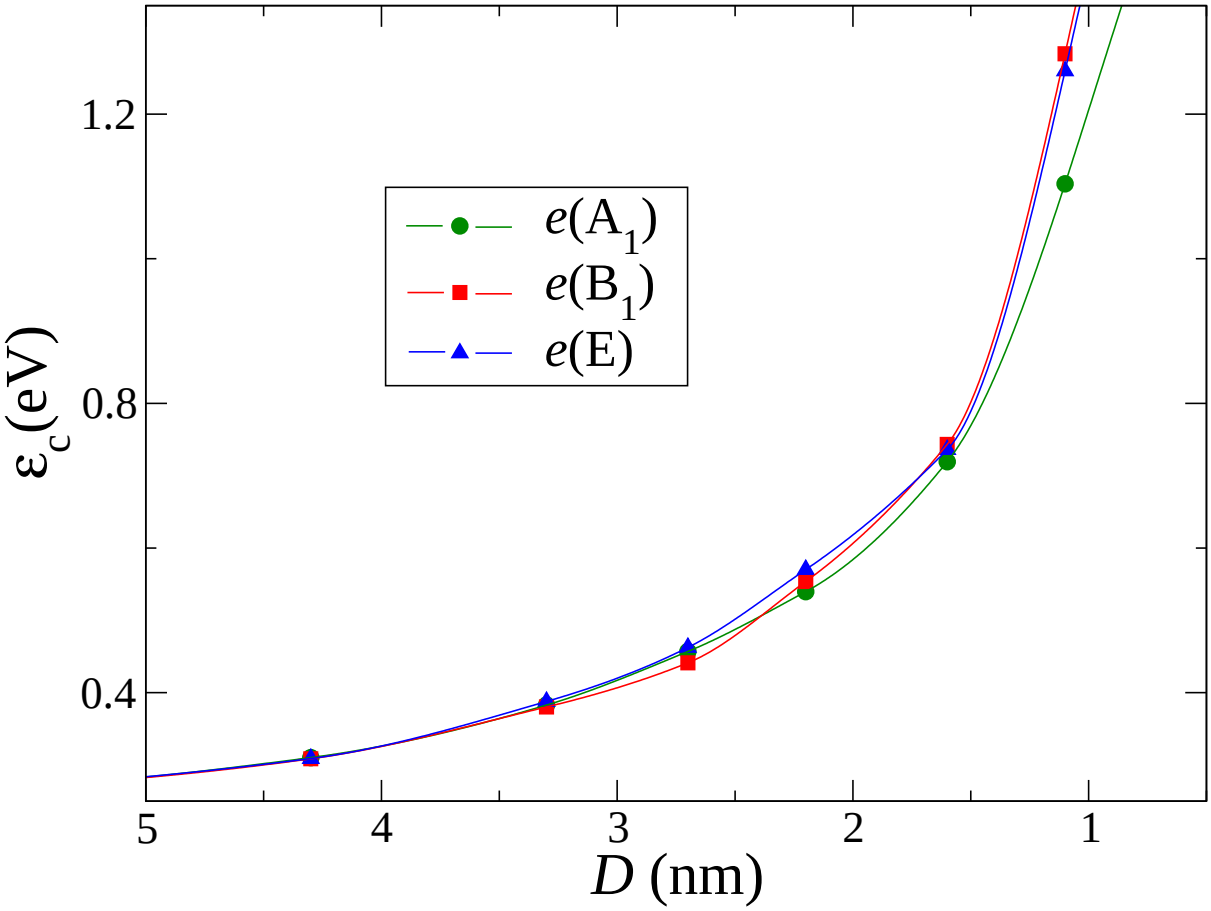

FIG. 2: (color online) Evolution of energies and symmetries of conduction band-edge states with decreasing diameters in Si [001] wires. One can clearly see the symmetry change sequence of the LUMO state with decreasing diameters: from degenerate A_1+B_1+E to B_1, and to A_1.

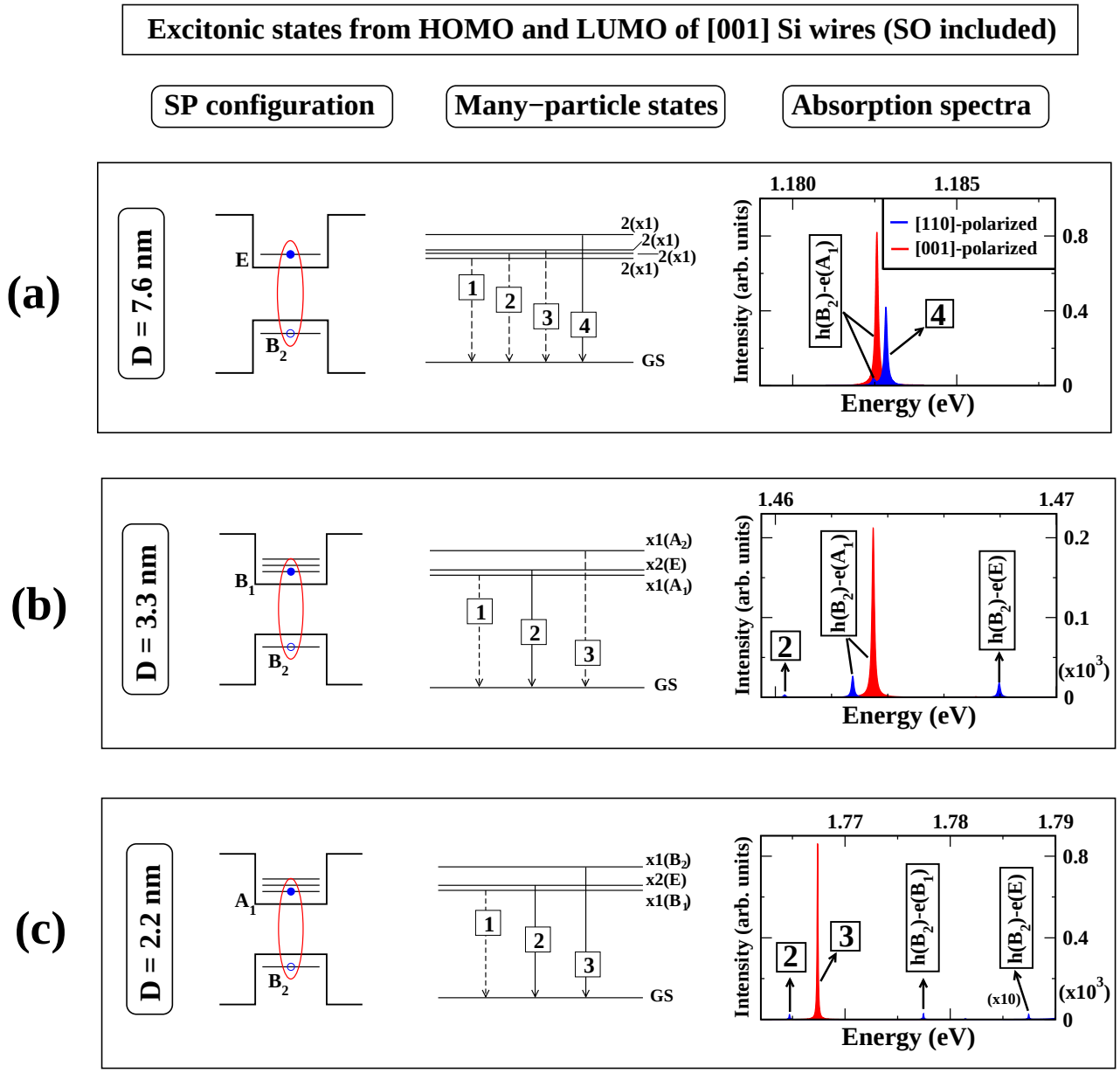

FIG. 3: (color online) Many-body excitonic states generated from HOMO⊗LUMO and absorption spectra for [001] Si wires at $D = 7.6$ (a), 3.3 (b), and 2.2 nm (c). The effect of spin-orbit coupling is included. Dash arrow-lines represent spin-forbidden transitions whereas solid arrow-lines represent spin-allowed transitions. The GS refers to the ground state after electron-hole recombination. The notations "1", "2", "3" and "4" mean the order of excitonic transitions from lower energy to higher energy in individual exciton group. The transition "1" corresponds to the ground excitonic state (excitonic gap). The effect of dielectric mismatch on excitonic energies is neglected as noted in the Method part.

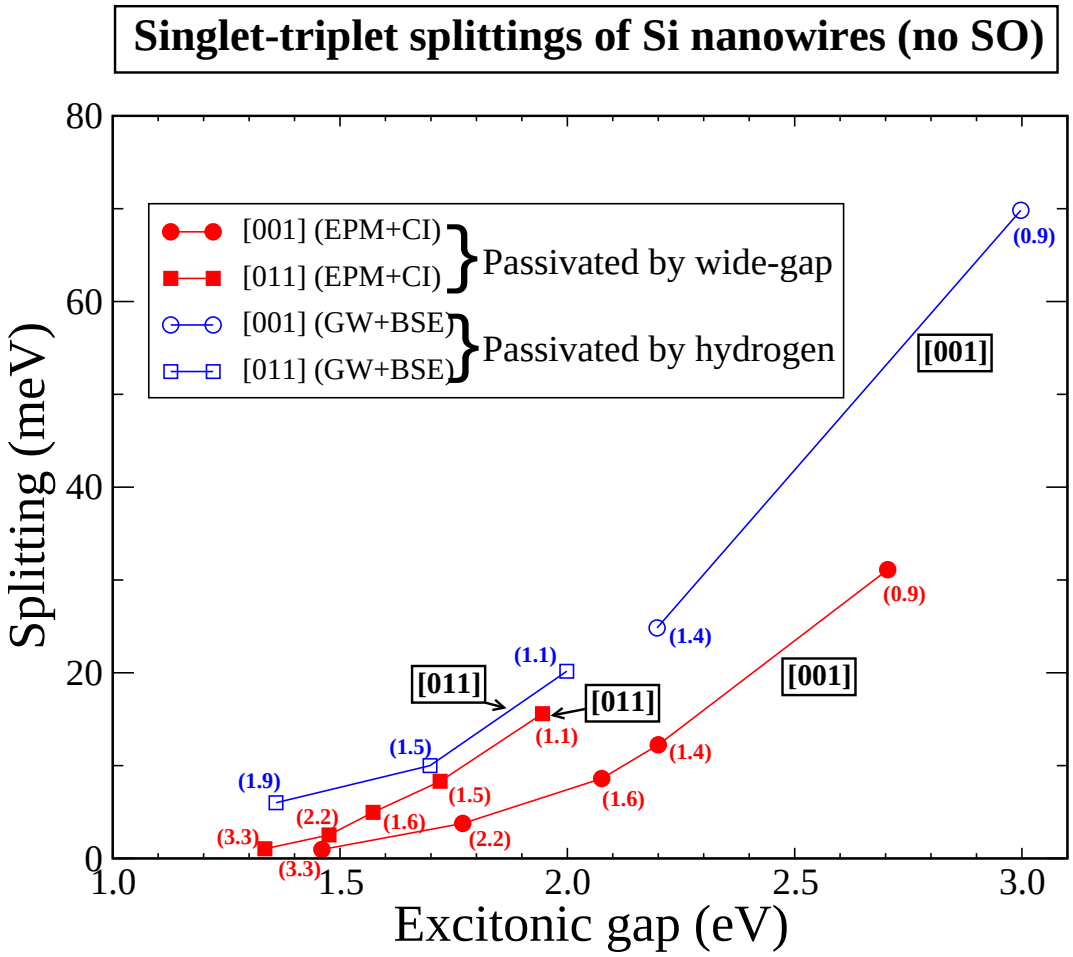

FIG. 4: (color online) Calculated excitonic-gap dependence of the singlet-triplet splitting Δ_{ST} (without including spin-orbit coupling) based on the HOMO and LUMO state in Si [001] and [011] wires, compared to GW+BSE results (Ref. 30). The wire diameter value is marked onto individual data point. For same-diameter points, we construct the same wire cross-section as Ref. 30 (not circular), while for larger diameter wires we use the circular cross-sections.

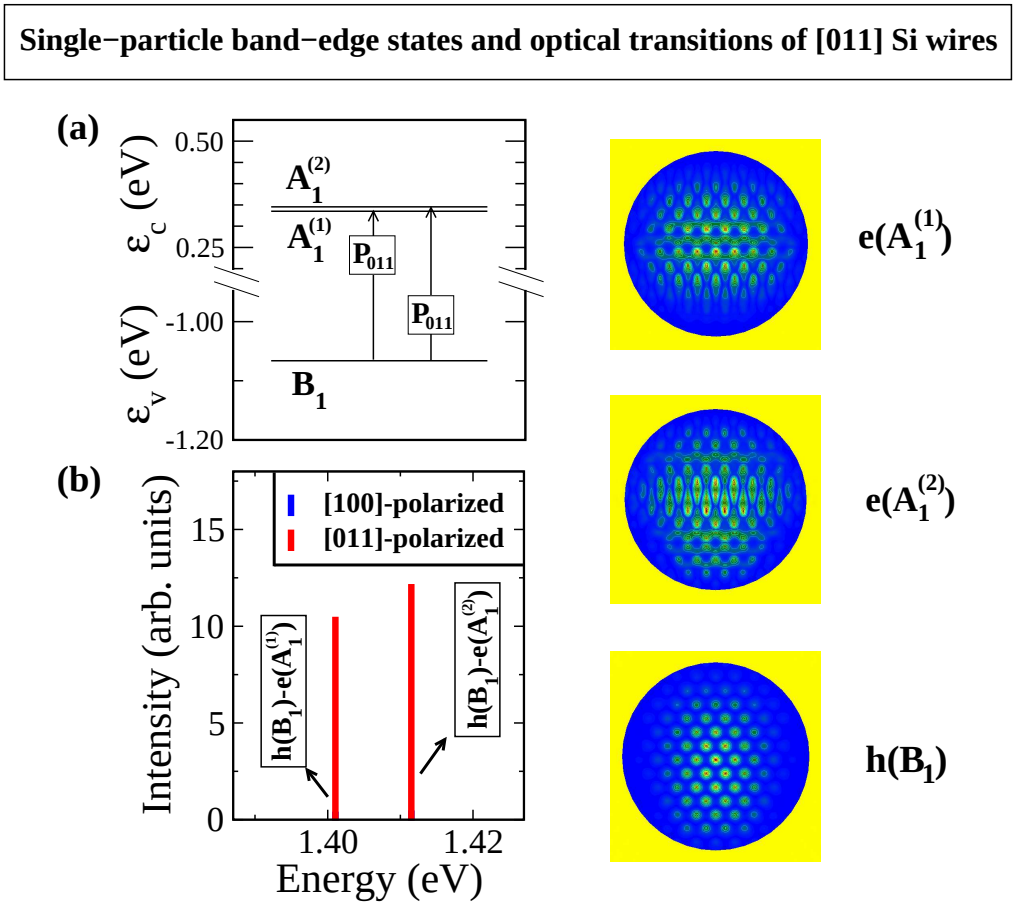

FIG. 5: (color online) Single-particle band-edge energy levels (a), corresponding optical transitions (b), and wavefunction amplitudes (right panel) for [011] Si wires of diameter $D = 3.3$ nm. The asymmetry of wavefunctions originate from the fact that the x and y direction of [011] wires are not equivalent, thus resulting in different confinement behaviors.

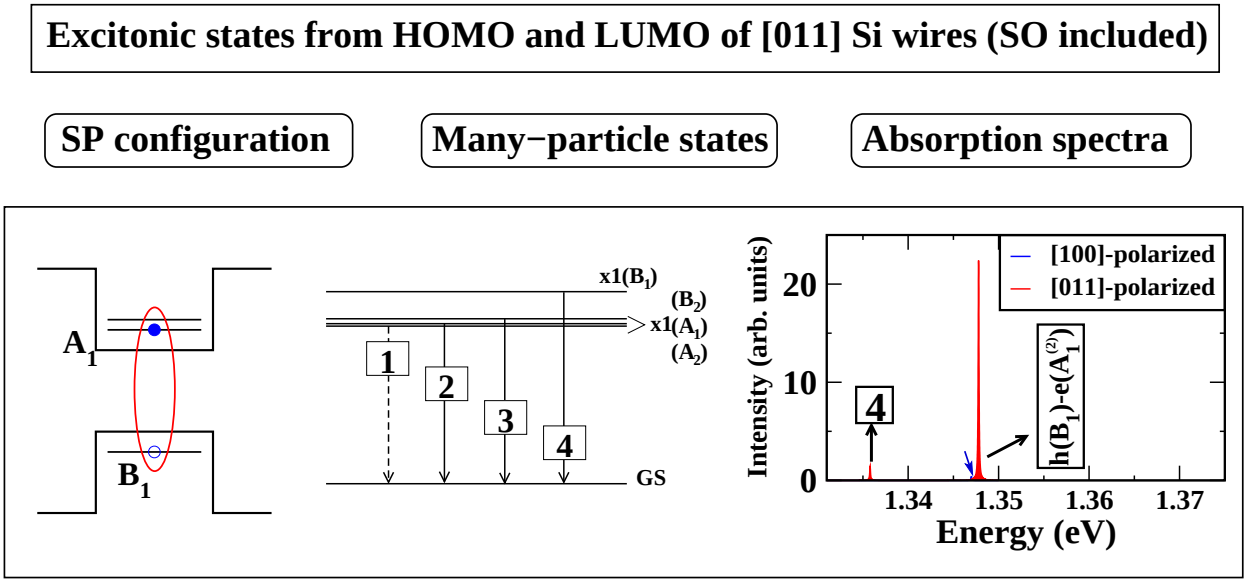

FIG. 6: (color online) Many-body excitonic structure and absorption spectrum generated from HOMO⊗LUMO for [011] Si wires of diameter $D = 3.3$ nm.

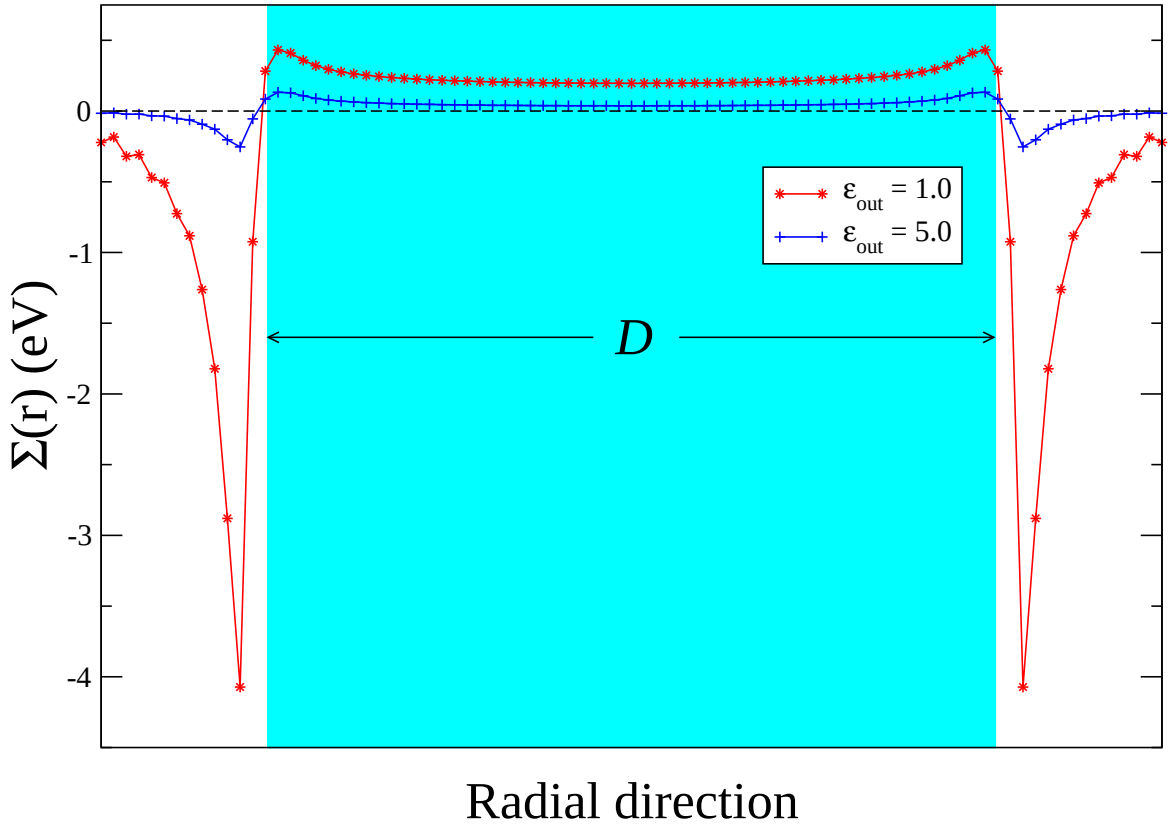

FIG. 7: (Color online) The numerically calculated surface-polarization potential $\Sigma(r)$ of a Si wire ($D = 3.3$ nm) is shown along the radial direction, for two values of macroscopic dielectric constant of the surrounding material ($\epsilon_{\rm out} = 1.0$, 5.0).

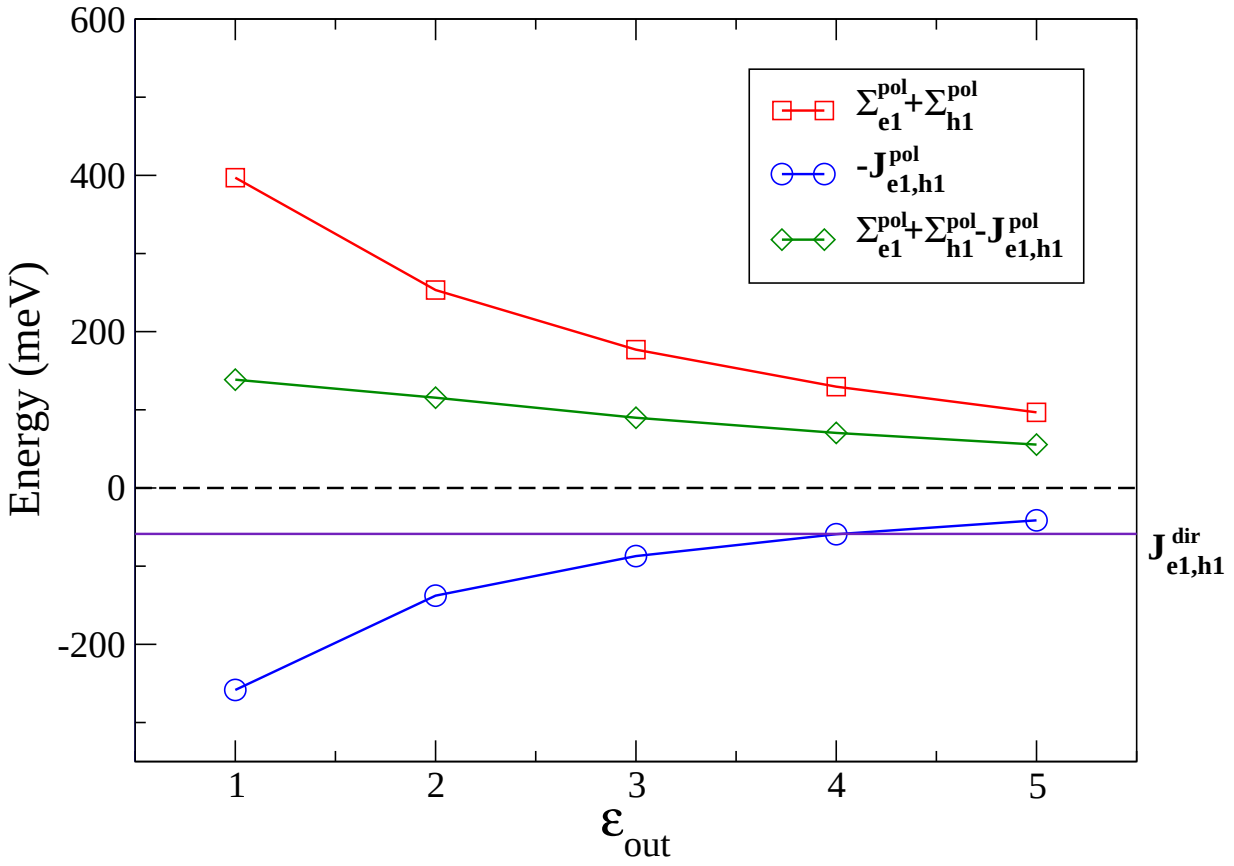

FIG. 8: (Color online) The surface-polarization-induced self-energy, $\Sigma_i^{\rm pol}$ (i = e1 (LUMO) and h1 (HOMO)), Coulomb interaction, $-J_{e1,h1}^{\rm pol}$ (negative value means decreasing exciton energies), and the sum $\Sigma_{e1}^{\rm pol} + \Sigma_{h1}^{\rm pol} - J_{e1,h1}^{\rm pol}$ are shown as a function of $\epsilon_{\rm out}$ for a [001] wire of diameter $D = 3.3$ nm. The direct Coulomb interaction (excluding surface-polarization effect), $J_{e1,h1}^{\rm dir}$ is shown as a solid (horizontal) line for comparison.

Tables

TABLE I: Direct product of interband dipole matrix elements, $\langle h|\mathbf{P}_i|e\rangle$ in Si [001] wires (D_{2d} symmetry) and [011] wires (C_{2v} symmetry). $\mathbf{P}_i$ represents the dipole operator along the wire axis (P_{001} for [001] wires and P_{011} for [011] wires) and in-plane direction (P_{110} for [001] and P_{100} for [011]). The symmetric A_1 representation (dipole-allowed transition) is given in bold. For [001] wires the LUMO A_1 is allowed in P_{001} and E is allowed in P_{110}. For [011] wires A_1 is allowed in P_{011}.

[001]:		
	$\langle h\|P_{001}(B_2)\|e\rangle$	$\langle h\|P_{110}(E)\|e\rangle$
	$\langle B_2 \otimes B_2 \otimes A_1\rangle = \mathbf{A_1}$	$\langle B_2 \otimes E \otimes A_1\rangle = E$
	$\langle B_2 \otimes B_2 \otimes B_1\rangle = B_1$	$\langle B_2 \otimes E \otimes B_1\rangle = E$
	$\langle B_2 \otimes B_2 \otimes E\rangle = E$	$\langle B_2 \otimes E \otimes E\rangle = \mathbf{A_1} \oplus A_2 \oplus B_1 \oplus B_2$
[011]:		
	$\langle h\|P_{011}(B_1)\|e\rangle$	$\langle h\|P_{100}(A_1)\|e\rangle$
	$\langle B_1 \otimes B_1 \otimes A_1\rangle = \mathbf{A_1}$	$\langle B_1 \otimes A_1 \otimes A_1\rangle = B_1$

TABLE II: Symmetry analysis of the excitonic states generated from HOMO and LUMO single-particle orbitals of [001] and [011] Si wires. Single-group representations are converted to corresponding double-group representations to include the spin degree of freedom for excitons.

	HOMO	LUMO	Excitons (HOMO⊗LUMO)
[001]:			
$D = 7.6$ nm	$B_2 \longrightarrow \Gamma_6$	$E \longrightarrow \Gamma_6 + \Gamma_6$	$\Gamma_6 \otimes \Gamma_6 = A_1 \oplus A_2 \oplus E$
$D = 3.3$ nm	$B_2 \longrightarrow \Gamma_6$	$B_1 \longrightarrow \Gamma_6$	$\Gamma_6 \otimes \Gamma_6 = A_1 \oplus A_2 \oplus E$
$D = 2.2$ nm	$B_2 \longrightarrow \Gamma_6$	$A_1 \longrightarrow \Gamma_7$	$\Gamma_6 \otimes \Gamma_7 = B_1 \oplus B_2 \oplus E$
[011]:			
$D = 3.3$ nm	$B_1 \longrightarrow \Gamma_5$	$A_1 \longrightarrow \Gamma_5$	$\Gamma_5 \otimes \Gamma_5 = A_1 \oplus A_2 \oplus B_1 \oplus B_2$

TABLE III: Calculated ground-state exciton energy E(i) and exciton fine-structure splittings for [001] wires (Fig. 3) and [011] wires (Fig. 6). E(i, i = 1, 2, 3, and 4) represent the energy of excitonic transition corresponding to the notation (1, 2, 3, and 4) in Fig. 3 and 6.

	[001]:			**[011]:**
D (nm)	7.6	3.3	2.2	3.3
E(1) (eV)	1.182	1.460	1.764	1.335
E(2)-E(1) (μeV)	21.3	238.9	399.4	3.4
E(3)-E(2) (μeV)	25.1	721.3	2668.6	20.8
E(4)-E(3) (μeV)	92.4			1017.6